AGU PUBLICATIONS

Journal of Advances in Modeling Earth Systems

RESEARCH ARTICLE

10.1002/2016MS000652

Simulating effects of a wind-turbine array using LES and RANS

Brian J. Vanderwende[1,2], Branko Kosović[3], Julie K. Lundquist[1,4], and Jeffrey D. Mirocha[5]

[1]Department of Atmospheric and Oceanic Sciences, University of Colorado, Boulder, Colorado, USA, [2]Now at National Center for Atmospheric Research, Boulder, Colorado, USA, [3]National Center for Atmospheric Research, Boulder, Colorado, USA, [4]National Renewable Energy Laboratory, Golden, Colorado, USA, [5]Lawrence Livermore National Laboratory, Livermore, California, USA

Key Points:
- WRF enables LES and RANS turbine array simulation using same dynamics
- Explicit *TKE* source is required for accurate *TKE* using the mesoscale scheme
- Wind-farm model lags LES in growth of wind-turbine array boundary layer

Correspondence to:
B. Vanderwende,
vanderwb@colorado.edu

Citation:
Vanderwende, B. J., B. Kosović, J. K. Lundquist, and J. D. Mirocha (2016), Simulating effects of a wind-turbine array using LES and RANS, *J. Adv. Model. Earth Syst.*, *8*, 1376–1390, doi:10.1002/2016MS000652.

Received 15 FEB 2016
Accepted 4 AUG 2016
Accepted article online 8 AUG 2016
Published online 27 AUG 2016

Abstract Growth in wind power production has motivated investigation of wind-farm impacts on in situ flow fields and downstream interactions with agriculture and other wind farms. These impacts can be simulated with both large-eddy simulations (LES) and mesoscale wind-farm parameterizations (WFP). The Weather Research and Forecasting (WRF) model offers both approaches. We used the validated generalized actuator disk (GAD) parameterization in WRF-LES to assess WFP performance. A 12-turbine array was simulated using the GAD model and the WFP in WRF. We examined the performance of each scheme in both convective and stable conditions. The GAD model and WFP produced qualitatively similar wind speed deficits and turbulent kinetic energy (*TKE*) production across the array in both stability regimes, though the magnitudes of velocity deficits and *TKE* production levels were underestimated and overestimated, respectively. While wake growth slowed in the latter half of the WFP array as expected, wakes did not approach steady state by the end of the array as simulated by the GAD model. A sensitivity test involving the deactivation of explicit *TKE* production by the WFP resulted in turbulence levels within the array well that were below those produced by the GAD in both stable and unstable conditions. Finally, the WFP overestimated downwind power production deficits in stable conditions because of the lack of wake stabilization in the latter half of the array.

1. Introduction

Continued growth in both the size and number of wind farms worldwide has motivated investigation into wind-turbine wake properties and the interactions among multiple wakes. High resolution large-eddy simulation (LES) models enable realistic reproduction of wake structure and evolution [e.g., *Crespo et al.*, 1999]. In LES models, turbines may be represented with actuator-disk models, which represent the turbine rotor as a solid body, or more computationally expensive actuator-line models [*Churchfield et al.*, 2012a], which represent the effect of each individual turbine blade. These turbine parameterizations have been used to analyze wake turbulence [*Jimenez et al.*, 2007, 2008], the wind speed deficit within offshore wakes [*Barthelmie et al.*, 2006; *Vollmer et al.*, 2015], tip vortices in the wake caused by blade rotation [*Troldborg et al.*, 2010], stability impacts on wakes [*Troldborg et al.*, 2011; *Lu and Porté-Agel*, 2011; *Mirocha et al.*, 2014; *Aitken et al.*, 2014; *Bhaganagar and Debnath*, 2014], wake effects on surface fluxes [*Calaf et al.*, 2011], and variations in wind turbine layout [*Meyers and Meneveau*, 2012; *Archer et al.*, 2013].

Though LES models can resolve fine scale wake structure, such detail comes at great computational cost, due to the requirements of fine mesh spacing and small integration time steps [*Churchfield et al.*, 2012b]. Therefore, many studies of large or multiple wind farms utilize parameterizations of wind-farm effects on Reynolds-averaged Navier-Stokes (RANS) flow. These parameterizations take one of the two forms: an effective roughness-length which retards the flow at the surface within the wind farm [e.g., *Keith et al.*, 2004], or an elevated momentum sink which extracts power from winds at realistic heights within the rotor-swept area [e.g., *Baidya Roy et al.*, 2004]. In the latter approach, turbulence can be explicitly added by the parameterization [e.g., *Fitch et al.*, 2012], or implicitly generated through the creation of shear within the rotor layer [e.g., *Jacobson and Archer*, 2012]. These wind-farm models have been used to simulate wake impacts on local hydrometeorology [*Baidya Roy*, 2011; *Fitch et al.*, 2013a], investigate the aggregate effect of wind power on regional and global climate [*Kirk-Davidoff and Keith*, 2008; *Fiedler and Bukovsky*, 2011; *Wang and Prinn*, 2011; *Vautard et al.*, 2014; *Fitch*, 2015a], evaluate the sensitivity of wind-farm output to surface characteristics [*Vanderwende and*

Lundquist, 2015], and estimate global wind resources [*Lu et al*., 2009; *Marvel et al*., 2013; *Jacobson and Archer*, 2012; *Adams and Keith*, 2013].

Despite the wide application of wind-farm parameterizations, few validations of these models have been performed. One reason for the dearth of validations is the difficulty of obtaining measurements of power output and meteorological quantities across large-wind farms. Observational coverage is required across the entire farm, as large farms can produce unique features not found in small arrays. For example, wind-turbine array boundary layers (WTABL), in which wake effects asymptote as the flow field equilibrates to the forcing from the turbines [*Calaf et al*., 2010], can form in the interior of utility scale wind farms. *Jiménez et al*. [2015] utilized turbine controls data from the offshore Horns Rev wind farm to investigate wind-farm parameterization (WFP) performance, and found reasonable agreement with the observations. *Cervarich et al*. [2013] suggested, through comparison with satellite observations of surface temperatures, that wind-farm models could reproduce spatial patterns of observed wake effects, but not their magnitudes. Another approach to validation compares RANS wind-farm parameterizations with LES simulations of multiple turbines. *Calaf et al*. [2010] used an LES model to evaluate various roughness-based representations of a moderately sized wind farm, and proposed a revised model to address discovered shortcomings. Recently, *Abkar and Porté-Agel* [2015a] tested a WFP with neutral LES simulations of large-wind farms, and found that the mesoscale wind-farm model was able to accurately represent wind farm wakes resulting from various turbine configurations.

However, no investigation of elevated-drag-wind-farm-parameterization performance in multiple stability regimes has been attempted. A number of studies have shown that both power output and wakes can vary significantly with stability [e.g., *Wharton and Lundquist*, 2012; *Vanderwende and Lundquist*, 2012; *Abkar and Porté-Agel*, 2015b; *Dörenkämper et al*., 2015]. With the additions of an elevated-drag wind-farm model for RANS simulations [*Fitch et al*., 2012] and a generalized actuator disk (GAD) turbine model for LES simulations [*Mirocha et al*., 2014; *Aitken et al*., 2014], the Weather Research and Forecasting (WRF) model is a suitable platform to conduct this evaluation.

Here, we evaluate the mesoscale WFP by comparing its output to coarsened, averaged output from the actuator-disk model in WRF-LES. In section 2, we present the LES and mesoscale domains and specify utilized physics options. We compare the performance of the WFP to GAD model output for convective and stable conditions in section 3, and assess the impact of various model settings on performance in section 4. Finally, we explore the ability of the WFP to model turbine array power output in section 5. Study implications and future research avenues are discussed in section 6.

2. Domain and Physics Setup

WRF v3.4 was utilized for all simulations, as it is currently the only version of the code with implementations of both the GAD model and a publicly available WFP. WRF is a fully compressible, nonhydrostatic model featuring a multitude of community-contributed parameterizations for various atmospheric physics processes, including the land-surface, clouds, radiation, diffusion, and mixing [*Skamarock et al*., 2008]. WRF is typically used for mesoscale simulation and numerical weather prediction, but recent versions also include an LES mode that has been validated across a range of forcing conditions [e.g., *Moeng et al*., 2007; *Mirocha et al*., 2010; *Kirkil et al*., 2012; *Lundquist et al*., 2012; *Mirocha et al*., 2013]. We utilized the GAD model, implemented into WRF-LES, to represent individual turbine wakes. The GAD model has been validated against scanning lidar observations of turbine wakes for both convective [*Mirocha et al*., 2014] and stable [*Aitken et al*., 2014] boundary-layer conditions [*Mirocha et al*., 2015]. These prior evaluations of the GAD model allowed us to use it as a reference wake state to compare with output from the wind-farm parameterization.

In WRF, the wind-farm parameterization represents the aggregate effects of turbine arrays on the flow with an elevated momentum sink and turbulent kinetic energy (*TKE*) source within the turbine-rotor layer [*Fitch et al*., 2012], with parameters dependent on the type of turbine being simulated [*Fitch*, 2015b]. In a study of performance over one diurnal cycle, *Fitch et al*. [2013a] found that the WFP produced near-surface temperature perturbations similar to those from LES simulations of wind-farm impacts on flow. The WFP correctly places the wind-farm momentum deficit above the ground, and reproduces observed secondary flow features such as near-surface wind speed increases in stable conditions [*Fitch et al*., 2013b]. Initial comparisons of the WFP to measured wake-induced power deficits at the Horns Rev offshore wind farm have produced

favorable results [*Jiménez et al*., 2015]. In version 3.6 of the WRF model, the WFP received a major update that, among other small changes, alters the method by which turbine specifications are input to the scheme. To best represent current model performance, we have ported this updated version of the WFP to WRF v3.4.

Both the GAD model and the WFP can be configured to represent simplified versions of any modern horizontal-axis turbine. We specified a hypothetical array comprised of 12 1.5 MW PSU Generic turbines (a turbine with similar specifications [*Schmitz*, 2012] to the proprietary GE 1.5 MW SLE turbine), separated by 11.6 D (rotor diameters) in the streamwise direction and 2.7 D in the cross-stream direction. This configuration represents a subset of turbines on the windward side of a large-wind farm. All simulations featured an outer turbine-free domain with periodic boundaries in which outflow returns on the opposite boundary as inflow. This configuration allowed for undisturbed flow features to fully develop during repeated passes through the outer domain, free from the perturbations of the turbine wakes that were solely contained within the inner domain. The turbine array was located near the center of the inner domains, which received boundary conditions from the outer periodic grid. The WRF model was initialized with no moisture, and microphysics, radiation, land-surface, and cumulus parameterizations were disabled. These simplifications were justified by the quiescent weather conditions observed during the original case study periods [*Mirocha et al*., 2014; *Aitken et al*., 2014].

To explore the wide range of operating conditions observed within wind farms [e.g., *Vanderwende and Lundquist*, 2012], we performed two LES simulations, one with convective conditions and another with stable conditions. These simulations were configured following the methodology of *Mirocha et al*. [2014] and *Aitken et al*. [2014] for the convective and stable cases respectively. The convective simulation featured 10 m resolution in all dimensions, and used Smagorinsky subfilter-scale closure to represent small turbulent motions. Unstable conditions were prescribed using a 100 W m^{-2} surface flux. The convective simulation was initialized with a uniform geostrophic wind profile of $u = 14.16$ m s^{-1} and $v = -3.14$ m s^{-1}, which yielded an average hub-height $U \approx 12.12$ m s^{-1} after spin-up adjustments were complete. In the stable simulation, a 5 m grid resolution was used with the nonlinear backscatter anisotropy (NBA) subfilter-scale closure. The use of NBA was motivated by the challenges in simulating the stable boundary layer [*Mahrt*, 2014], for which the NBA closure scheme was designed [*Kosović*, 1997]. The stable condition was maintained by a 0.2 K h^{-1} surface cooling rate, following *Aitken et al*. [2014]. A uniform geostrophic wind profile of $u = 7.09$ m s^{-1} and $v = -2.44$ m s^{-1} was used, producing an average hub-height $U \approx 6.5$ m s^{-1} after spin-up. In both simulations, we prevented turbulence from reaching the top of the model domain by specifying a 10 K km^{-1} temperature inversion and using a Rayleigh damping layer. In the stable simulation, a stronger capping inversion develops as the lower levels of the boundary-layer cool over time.

Two mesoscale simulations were performed with configurations designed to emulate the mean environment of the GAD model cases. At heights also covered by the LES domains, the same wind and temperature profiles were imposed (including the 10 K km^{-1} capping inversions) so that mean profiles after model spin-up closely matched those of the LES simulations. Above the LES domain model-tops (1700 m in the convective case and 646 m in the stable case), a 3 K km^{-1} inversion was imposed throughout the rest of the troposphere. Domain grids were aligned so that the turbines in the LES domain would fall within distinct RANS grid cells in the along-wind direction. The WFP was tested at 900 and 300 m horizontal resolution for all mesoscale configurations, which enabled evaluation of performance scaling with grid spacing.

The spatial dimensions and selected physics options for all model runs are summarized in Table 1. The domains, approximate turbine locations, and thermodynamic profiles appear in Figure 1. We used 4 h of simulation time after varying spin-up lengths to generate the following results. To compare the LES and mesoscale outputs using equivalent parameters, we averaged the areas of the LES domains contained within each relevant mesoscale grid cell temporally and spatially to match the resolution of the mesoscale model output. Therefore, results from the GAD model are presented as equivalent mesoscale output for areas equivalent to the upstream inflow, the six turbine rows, and the downstream outflow mesoscale grid cells. At 900 m resolution, *each row* of turbines is located within a unique mesoscale-equivalent grid cell area, while at 300 m, *each turbine* has its own unique cell area.

To evaluate WFP performance in situations relevant to contemporary studies [e.g., *Jiménez et al*., 2015], we performed two additional RANS simulations (Table 1). We doubled the vertical resolution of the mesoscale

Table 1. LES and RANS Model Configurations

			Domain specifications				
Name	Stability or unique setting	Subfilter/PBL scheme	$L_{x,y}$	$L_{z,rotor}$	N_x	N_y	N_z
Large-eddy simulation scales							
GAD	Convective	Smagorinsky	10 m	10 m	505	121	64
GAD	Stable	NBA	5 m	5 m	706	181	75
Reynolds-averaged Navier-Stokes scales							
DEF	Default WFP	MYNN 2.5	0.9, 0.3 km	18 m	100	61	50
HVR	Decreased L_z	MYNN 2.5	0.9, 0.3 km	9 m	100	61	55
NAT	No *TKE* source	MYNN 2.5	0.9, 0.3 km	18 m	100	61	50

grid in the rotor layer (the high vertical resolution, or HVR, runs) to determine the effect of enhanced fidelity on vertical wake mixing and momentum entrainment. We investigated the importance of explicit *TKE* generation by turning off the *TKE* source in the WFP (the no added turbulence, or NAT, runs). This test was motivated by the existence of elevated-drag wind-farm parameterizations that do not explicitly add *TKE*, but rather depend on shear-instability to produce turbulence [e.g., *Jacobson and Archer*, 2012; *Abkar and Porté-Agel*, 2015a]. As with the default mesoscale configurations (the DEF runs), these two runs represented the turbine array on 900 and 300 m domains.

3. LES and Mesoscale Turbine Wakes in Two Stability Regimes

3.1. Hub-Height Wake Structure in the LES Simulations

Significant differences in LES wake structure exist between the convective and stable simulations, as shown by the maps of average hub-height wind speeds in Figure 2. These maps cover the area encompassed by the inflow, turbine array, and outflow mesoscale grid cells. The left and right edges of the plots correspond to the upwind and downwind sides of the domain, respectively. Wake deficits from upstream turbines influenced the inflow winds of downstream turbines in both stability regimes, though significant wake effects extended much further downstream in the stable simulation. In the convective regime, turbulent mixing eroded wakes, reducing the downwind propagation distance of discernable wake effects. This mixing also increased the lateral interaction of wakes downwind of the turbines in the convective simulation. The lateral

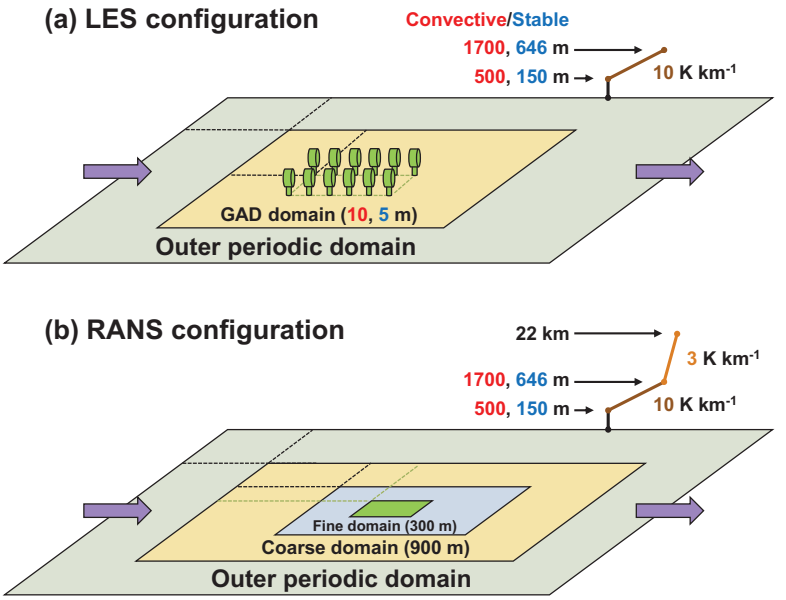

Figure 1. Graphical schemata of the (a) LES domain configuration and (b) RANS domain configuration. The relative locations of turbines and turbine-equivalent grid cells are shown in green. The mean inflow wind direction is indicated by the purple arrow. Initial thermodynamic profiles are provided for both configurations.

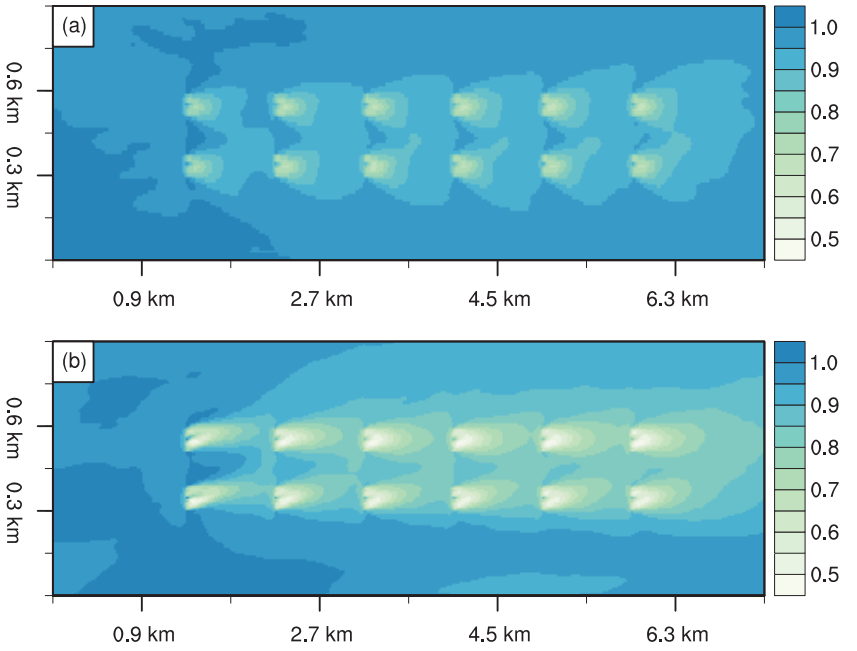

Figure 2. Normalized mean horizontal winds from the 4 h integration period after the end of model spin-up for LES runs with (a) convective and (b) stable boundary-layer conditions.

expansion in the convective case was also spurred by significant variations (up to 45°) in the mean wind direction, typical in conditions featuring transient large overturning turbulent eddies.

Crucial to this analysis, the mean turbine wake extents in both stability regimes remained laterally contained within the equivalent mesoscale cell areas (portions of the LES domain encompassed by each 900^2 m^2 mesoscale grid cell). However, all of the wakes in the stable simulation exhibited varying degrees of veering (rightward turning with distance). This wake veering/bending was caused by a combination of the rotation of the turbine rotors and wind veer with height present in the stable boundary layer wind profile. The effect intensified with each consecutive row, as additional turbine wakes entrained momentum from aloft (see Figure 3). Despite the downstream veering of winds, which was contained within the wakes themselves and not present in the background flow, no downstream turbines experienced undisturbed mean inflow. Downstream wind veering was not evident in the convective regime (not shown). The wind profile was well mixed in the convective case, and so this effect was not produced by the LES model.

3.2. Near-Rotor Profile Comparisons of Wind Speed and *TKE*

The LES simulations with the GAD model produced horizontal wind speed (U_H) profiles consistent with established boundary-layer theory [*Stull*, 1988]. As expected, larger wind speed deficits were produced in the stable simulations (Figure 4), as convective mixing will erode wakes more quickly in unstable regimes.

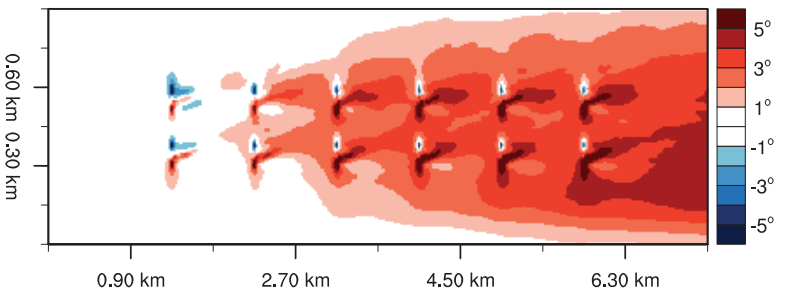

Figure 3. Mean wind direction change (°) relative to upstream inflow conditions for the 4 h period after model spin-up in the stable simulation.

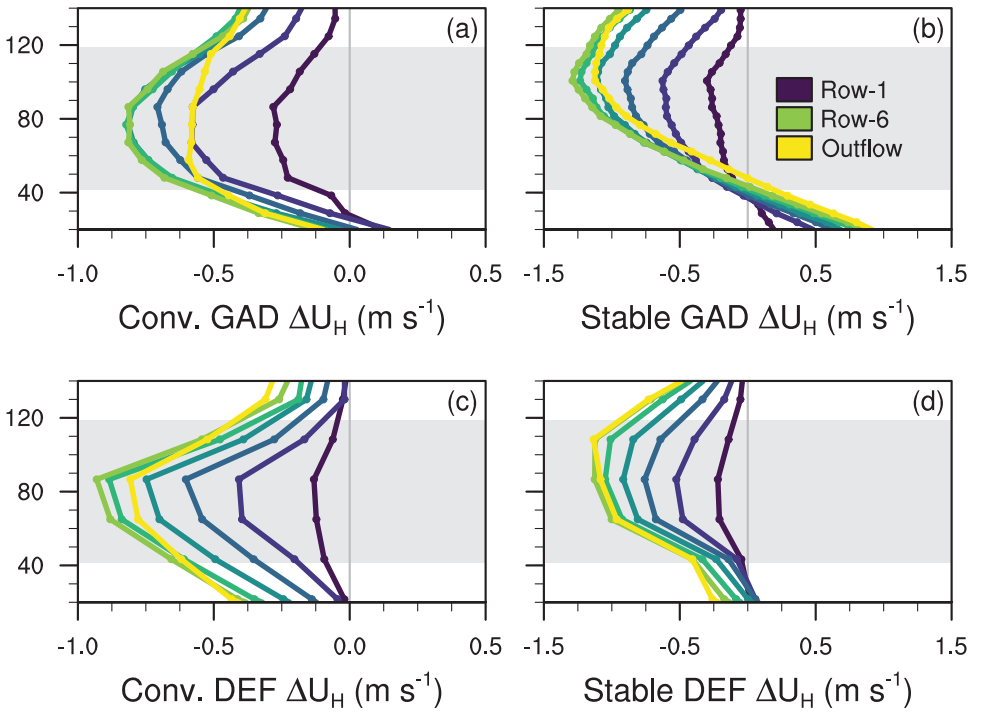

Figure 4. Low-level wind speed (U_H, m s^{-1}) profiles for the (a, b) GAD and (c, d) DEF configurations during (a, c) convective and (b, d) stable conditions. Values are shown relative to the inflow wind speed profile. Data are presented from seven 900^2 m^2 mesoscale grid cell areas representing conditions within the six rows of turbines and the array outflow outflow, respectively.

The 900 m grid mesoscale simulations were able to replicate this stability dependence, though stable deficits were underestimated within the latter turbine rows by the RANS output. The DEF simulations also correctly captured the impact of stability on the height of the maximum velocity deficit. In convective conditions, wake effects maximized around hub-height, while in stable conditions the maximum occurred in the upper half of the rotor layer around 100 m above ground level (AGL). In both the GAD and DEF simulations, velocity deficits stabilized in the last two rows, which indicates the formation of WTABL flow [e.g., *Calaf et al*., 2010].

The one major GAD feature that the DEF simulation did not replicate was flow acceleration below the rotor in the stable simulation (by up to 0.7 m s^{-1}). As a result, low-level shear within the wake was also underrepresented by the WFP. Such low-level speed increases have two potential causes: (1) enhanced turbulent mixing of higher-momentum air downward toward the surface and (2) winds becoming channeled below the rotor due to pressure perturbations. This below-rotor wind acceleration was observed in wind farm measurements by *Rajewski et al*. [2014]. Such effects are difficult to resolve with the (relatively) coarse grids used in mesoscale simulations, because the WFP distributes rotor drag over a larger area than the GAD model. Therefore, there is less flow blockage due to the turbines simulated by the WFP, resulting in less below-rotor momentum enhancement.

Disagreement increased between the GAD and DEF outputs for downwind *TKE* production, as shown in Figure 5. Increases in *TKE* occurred too rapidly in the convective DEF simulation, and significant production continued in the latter turbine rows, where WTABL flow should have been present. As a result, maximum hub-height *TKE* production was overestimated by nearly 50% relative to the GAD run in convective conditions. Meanwhile, maximum *TKE* increases were in better agreement for both models in stable conditions. Unfortunately, the early evolution of *TKE* in the wake was erroneously depicted by the WFP, as production was much too large in the first two turbine rows, relative to the GAD model. Because of this early production error, asymptotic WTABL behavior began by the third turbine row in the stable simulation, while it only appeared in the latter rows in the GAD simulation. Additionally, the WFP incorrectly placed the height of maximum production at hub level, while the GAD model produced *TKE* maxima in the upper half of the rotor disk. This result indicates that the vertical mixing estimated by parameterized *TKE* in the DEF

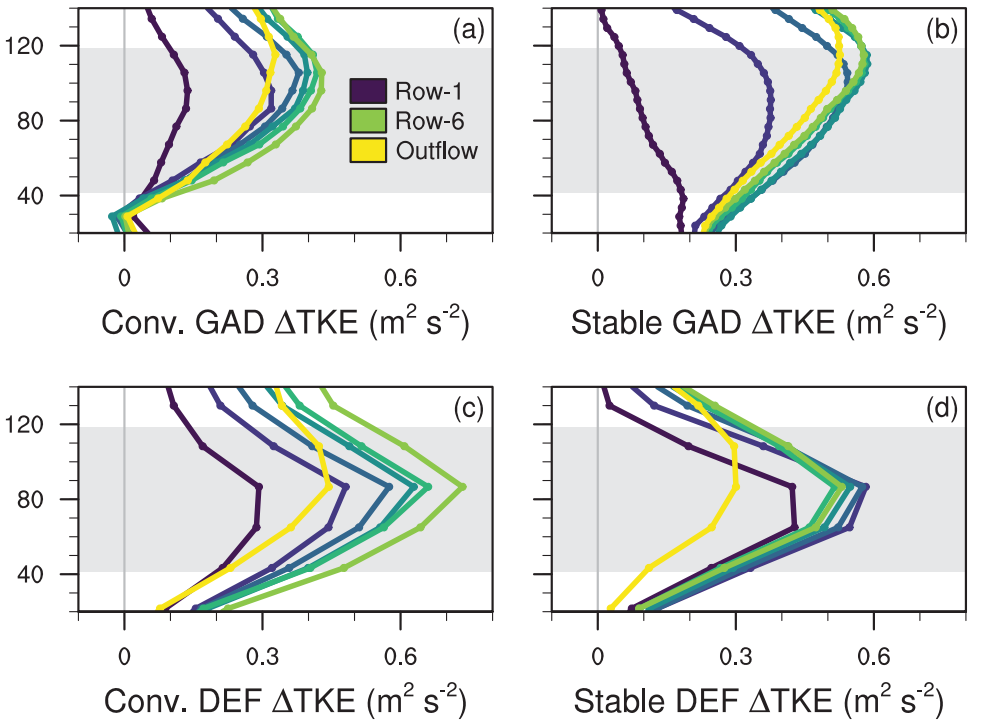

Figure 5. Low-level turbulent kinetic energy (*TKE*, $m^2\ s^{-2}$) profiles for the (a, b) GAD and (c, d) DEF configurations during convective (a, c) and stable (b, d) conditions. Values are shown relative to the inflow *TKE* profile.

simulation does not correctly represent the equivalent mixing caused by explicitly simulated *TKE* in the GAD simulation.

A prominent trend in the stable GAD simulations of both U_H and *TKE* changes was the increase in the height of the maxima as air flowed through the wind farm. For *TKE* changes, the maximum started at 15 m above hub-height in the second turbine row, and rose to 35 m above the hub by the sixth and final row of turbines. Maximum increases rose to even higher heights in the outflow grid cell, reaching levels above the top of the rotor. The DEF simulations were unable to replicate this vertical mixing; only in the outflow cells did any vertical displacement of the maxima occur. The amount of *TKE* also decreased rapidly in the DEF outflow cells, which strongly suggests excessive turbulence dissipation rates. In the absence of the direct turbine forcing, wake turbulence dissipated at rates far exceeding those simulated in the GAD runs. Meanwhile, outflow velocity deficits were in good agreement, suggesting that *TKE* losses due to vertical mixing were not the cause for the outflow cell errors.

3.3. Wind-Turbine Array Boundary Layer Flow

The use of six turbine rows allowed us to assess the development of wind-turbine array boundary layers as flow traversed the array. To illustrate the reduction in hub-height velocity deficits and turbulence production within the latter half of the array, row-by-row differences in both quantities are displayed in Figure 6. Row 1 values are relative to the inflow cells, not pictured here.

Asymptotic behavior began at different distances within the wind farm for velocity deficits and turbulence. The GAD output in Figure 6a demonstrates that *TKE* production began to asymptote to zero by row 3 in the convective case and row 4 in the stable case. Asymptotic behavior developed later for velocity deficits, only beginning after row 4 in convective conditions and perhaps by the end of the array in stable conditions. The general trend of decaying rates of change with downwind distance was replicated by the DEF runs, as shown for the 900 m grid in Figure 6b and the 300 m grid in Figure 6c. While the development of WTABL flow, or a lack-thereof, was similar using both mesoscale grid resolutions, the overall magnitude of wake impacts was larger in the finer-resolution runs. Asymptotic behavior was only observed for *TKE*, while U_H changes continued to decay to the end of the array. This result indicates that the WTABL developed more

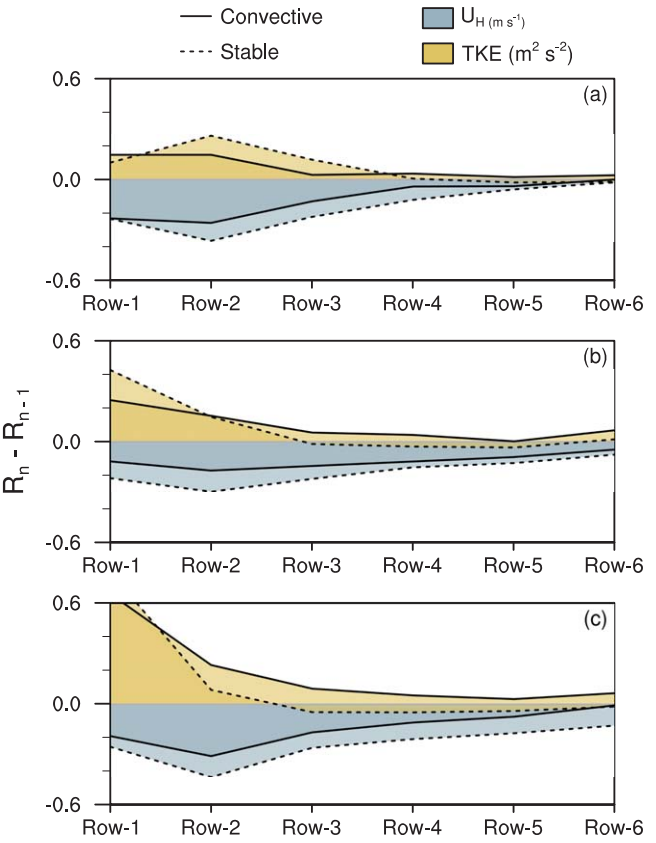

Figure 6. The rates of change of U_H and *TKE* between turbine rows for the (a) GAD, (b) DEF with 900 m grid, and (c) DEF with 300 m grid simulations. Convective results are indicated by solid lines and stable results by dashed lines.

slowly in the mesoscale simulation, thus yielding a larger overall wind and turbulence footprint for the wind farm, as downwind turbines were able to influence the flow more intensely in the DEF runs.

In the stable GAD simulation, changes in wind speed and turbulence reach maxima in the second row of turbines. This counterintuitive result is correctly replicated for U_H by the DEF runs, but they incorrectly produced maximum *TKE* changes within the first row. This error was caused by anomalously low background turbulence levels in the mesoscale simulation. Because ambient *TKE* was almost zero in the inflow cell area, the initial perturbation to the flow posed by the first row of turbines appears artificially high.

4. WFP Sensitivity to Model Configuration

Increasing the vertical resolution in the mesoscale rotor-layer (HVR run) and deactivation of explicit turbulence generation (NAT run) both produced mixed results when compared to the default WFP configuration. The performance of all three mesoscale configurations, relative to GAD output, was assessed using U_H, wind direction, and *TKE* for both stability regimes. First, deviations in all three variables relative to the unperturbed inflow cell were calculated for all four runs. Then, the mean signed difference between each mesoscale configuration and the corresponding GAD run was computed, and expressed as a percent of the reference GAD value in Table 2.

While mean errors varied significantly among the configurations, no particular configuration excelled in all metrics. The default WFP configuration underestimated the magnitude of downstream velocity deficits using 900 m resolution, as indicated by negative signed errors in both stability regimes. The NAT configuration reduced this error by 32% in the convective run and 47% in the stable run, as the loss of explicit *TKE* production slowed wake erosion, and thus allowed velocity deficits to grow larger. The same effect occurred for the 300 m resolution runs, though DEF errors were lower to begin with, and the loss of *TKE* in the NAT

Table 2. Mean Signed Error in Rates of Change Across the Array for U_H, Wind Direction, and *TKE*[a]

	900 m domain			300 m domain		
WFP setup	U_H (%)	*WD* (%)	*TKE* (%)	U_H (%)	*WD* (%)	*TKE* (%)
Convective						
DEF	−43.6	−389.7	55.0	−15.9	−280.0	231.4
HVR	−28.3	31.7	53.7	3.9	355.9	228.0
NAT	−29.5	−392.2	−96.2	2.5	−278.2	−79.4
Stable						
DEF	−27.7	−86.6	36.4	−5.4	−81.5	107.2
HVR	−31.6	−85.7	33.7	−10.3	−75.2	105.1
NAT	−14.6	−118.0	−94.8	12.1	−121.1	−90.1

[a]Errors are expressed as the percentage of GAD model values.

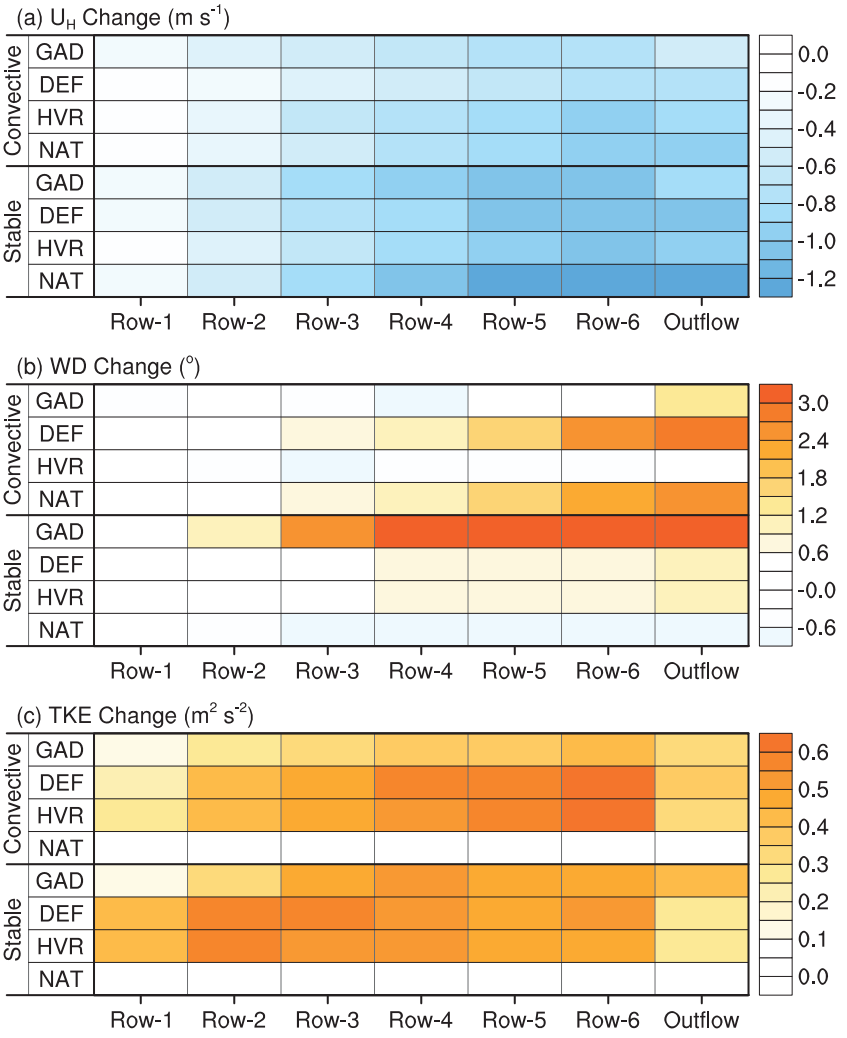

Figure 7. Summaries from various WRF configurations of downstream changes in hub-height (a) horizontal wind speed (U_H) (m s^{-1}), (b) wind direction (°), and (c) *TKE* (m^2 s^{-2}) for the 900 m mesoscale grid cell equivalent areas containing the six turbine rows and array outflow. All values are relative to the inflow cell.

run actually degraded performance in the stable regime. Meanwhile, most WFP configurations had difficulty simulating wind direction changes, with the 31.7% error for convective conditions using the HVR 900 m grid being the single anomalously accurate result. Note that because the convective GAD simulation produced very little veering, percent errors become magnified after normalization.

Unsurprisingly, changes in mesoscale *TKE* differed most strongly between the DEF and NAT configurations. At both grid resolutions, the DEF (and HVR) mesoscale runs produced excessive *TKE*, while the NAT simulation underrepresented turbulence relative to the GAD model. Increasing the vertical resolution had little effect on *TKE* values. Note how errors in turbulence increased for the default runs when moving to finer horizontal resolution, but decreased for the NAT configuration. This result may appear to support the argument for the NAT design, which holds that velocity-deficit induced shear will mechanically produce turbulence organically, eliminating the need for explicit *TKE* generation [*Jacobson and Archer*, 2012], but caveats apply. Recall that turbulence estimates from the NAT runs are only superior for the 300 m grid, a resolution that lies on the border between the mesoscale and LES—the so-called *terra incognita* [*Wyngaard*, 2004]. Therefore, it is perfectly reasonable to expect that the assumptions underlying the unmodified WFP will begin to break down at such fine scales. Additionally, some questions remain about the accuracy of *TKE* levels on nested LES grids. Turbulent dissipation may become decoupled from eddies at grid refinement boundaries, causing temporary overestimation of *TKE* levels [*Mirocha et al.*, 2013].

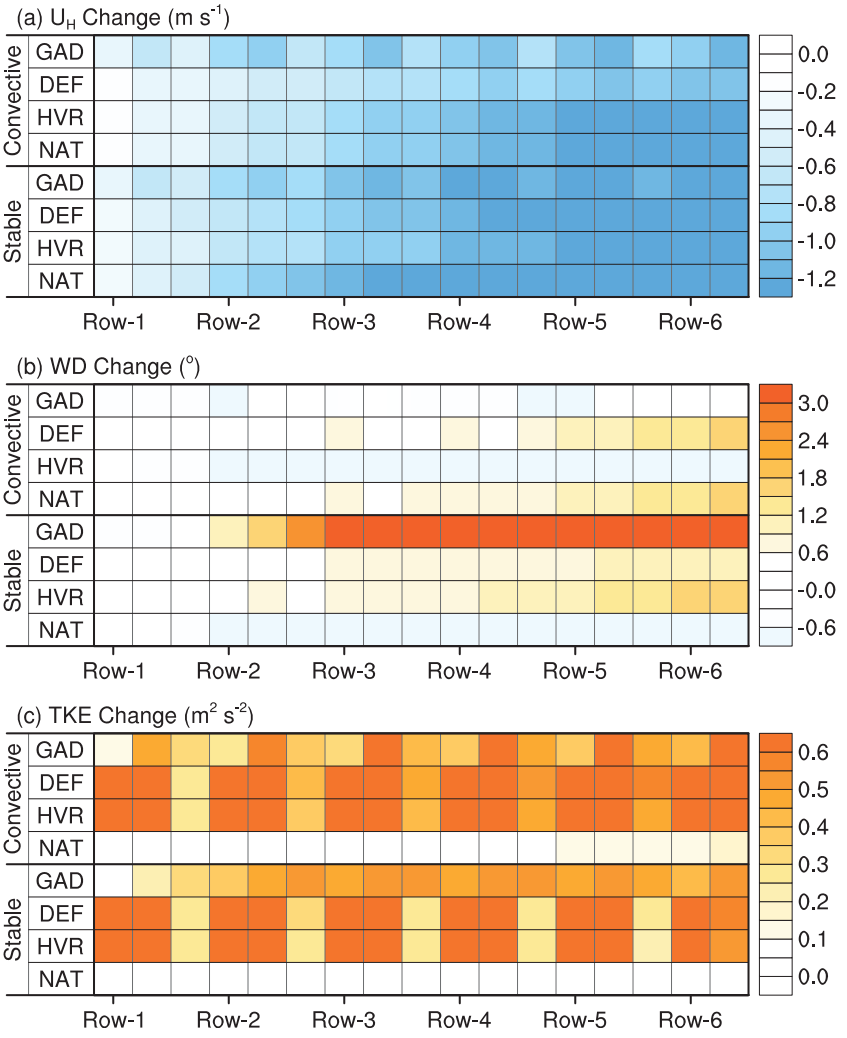

Figure 8. Same as Figure 7, but for the 300 m mesoscale grid cell equivalent areas.

The spatial distribution of wake effects for the GAD run and all three mesoscale configurations is visually depicted in Figure 7, showing changes in hub-height (a) U_H, (b) wind direction, and (c) *TKE*, relative to the inflow cell, for the six turbine rows and outflow mesoscale grid cells in all model configurations. The cells shown in this figure represent grid cell equivalent areas for the 900 m mesoscale domain. A similar visualization at 300 m is provided in Figure 8. Note that the number of cells has increased with finer horizontal resolution, and there are now two intermediate cells between each turbine row.

The use of hub-height transects enables detection of features that are not evident in the mean signed error statistics. For example, the recovery of wind speed was too small for the mesoscale outflow cells, relative to the GAD output. In the stable case, we can attribute this error to underestimation of *TKE* in the outflow cells, as evidenced by the poorer performance of the NAT runs in that cell. We also gain insight into the source of wind direction errors. In the convective case, the DEF and NAT configurations both produced anomalous veering, while the HVR simulation correctly kept direction changes small. Meanwhile, the veering present in the stable GAD simulation (and shown in Figure 3) was missed by all mesoscale configurations. Errors were largest for the NAT simulation, in which inadequate turbulent mixing precluded the entrainment of momentum from aloft.

The NAT runs produced turbulence fields that contrast sharply with those of the GAD output. In fact, there is no discernable signature of added turbulence at all in the NAT 900 m simulation, and only slight *TKE* generation in the latter cells of the 300 m convective run. These results indicate that disabling explicit *TKE*

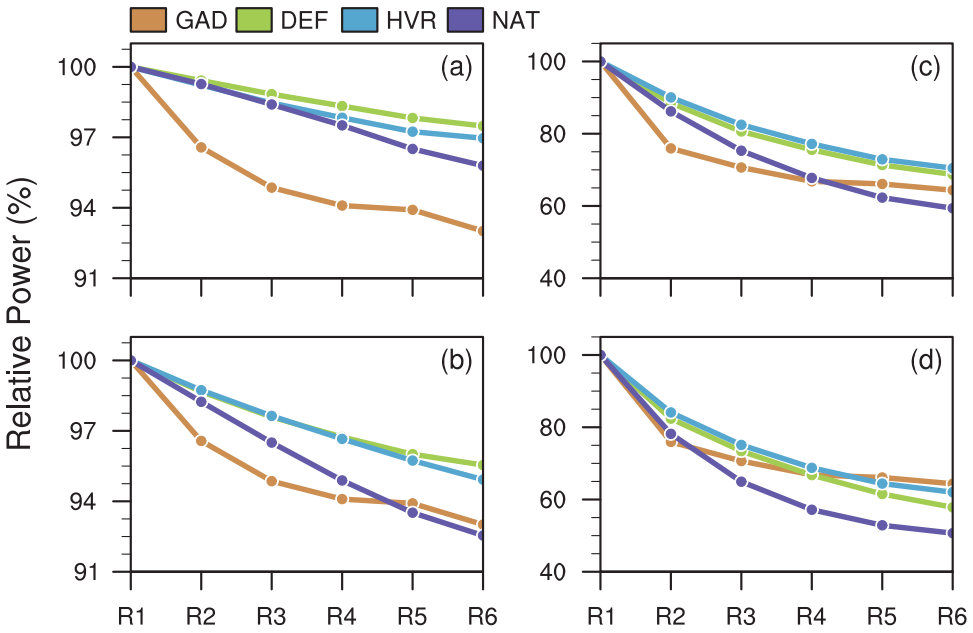

Figure 9. The power output for each row of the turbine array, relative to the power output of the initial upstream row. Results from each simulation are shown for the (a) 900 m and (b) 300 m convective cases, and the (c) 900 m and (d) 300 m stable cases.

production in the wind-farm parameterization produces unphysical results, and the statistical advantage enjoyed by the NAT runs for 300 m domain turbulence was a case of getting the right answer for the wrong reason. While the DEF configuration did overestimate *TKE* production by significant amounts, the qualitative signature of increased turbulence within the wind farm followed by decaying turbulence in the outflow cell follows our expectation from the LES results.

Lastly, the 300 m results provide the opportunity to analyze flow evolution between turbine rows. While these cells are not directly impacted by either the GAD model or the WFP, intermediate changes to the flow precondition behavior in the subsequent turbine row. In the GAD simulation, flow recovery occurred between each turbine row. For U_H, this behavior was only replicated by the default WFP configuration in convective conditions, and even then the magnitude of the recovery was underestimated. The DEF and HVR configurations reproduced *TKE* reductions between turbine rows, and even managed to capture the decaying magnitude of those reductions in the latter half of the array in convective conditions. The 300 m results do illustrate one flaw of the explicit *TKE* generation process—turbulence is generated in situ within the turbine containing grid cell. However, in the GAD simulation, not all turbulence is generated immediately within the turbine containing cell. *TKE* production actually maximizes in the cell subsequent to the turbine row, presumably due to mechanical production induced by increased wind shear.

5. Estimates of Turbine Power Production

Wind-farm parameterizations are primarily designed to study the impact of wind farms on regional and global momentum fields. However, some investigators have also used these models to estimate power output [e.g., *Jiménez et al.*, 2015], and they can be particularly useful for large-scale problems such as grid balancing [*Archer and Jacobson*, 2007; *St. Martin et al.*, 2015] and exploring interactions between wind farms [*Kaffine and Worley*, 2010; *Nygaard*, 2014]. We have examined its performance in this respect for both (a, b) convective and (c, d) stable regimes in Figure 9. All values indicate the percentage of power generated relative to the upwind turbine row. Power values were calculated for both the LES and mesoscale simulations by taking the inflow-cell wind speeds and using the turbine power curve to translate those speeds into an equivalent power output.

Power differences across the turbine array were small during convective conditions for all configurations. Total power reductions did not exceed 8% by row 6 in any run. This result highlights the importance of

inflow wind speed. When winds are above the rated wind speed for a turbine, power output becomes insensitive to inflow speed as the turbine blades pitch to maintain reliable power production. While average wind speeds during convective conditions were above the rated wind speed (12 m s^{-1}) throughout the array for both the LES and mesoscale simulations, the inflow to the GAD model turbines exhibited higher variance due to the finer spatiotemporal resolution of the LES domain. Therefore, there were more instances with wind speeds below the rated value for the turbines in the LES simulation, resulting in more significant power declines, particularly within rows 2 and 3.

Differences among the model configurations were larger in the stable simulation. Lower inflow wind speeds magnified effects on power output, as these wind speeds occur in the portion of the power curve where output rapidly rises with increasing inflow speed. All WFP configurations underestimated the power reductions in row 2 relative to the GAD model (75% at 900 m resolution), with the best performance from the NAT simulation (86%), and the worst from the HVR (90%). However, by row 6, the NAT simulation produced larger power reductions from row 1 than the GAD model run. This reversal occurred because of the aforementioned lack of asymptotic behavior in the mesoscale simulations, resulting in downwind-row power reductions that were too large. The lack of turbulent mixing amplifies this error in the NAT runs, yielding a row 6 relative power output of 50%, while the GAD model simulation row 6 output remained at 64%. At 300 m resolution (9d), the NAT simulation produces the best initial decline in power output, but in the later rows all other mesoscale configurations better match the GAD model run.

6. Conclusions

Mesoscale wind-farm parameterizations have the ability to represent the impacts of wind power generation on atmospheric boundary layer flow at regional and global scales. However, their performance has only been tested over a very limited set of flow conditions that do not represent those found in general operation. Large-eddy simulations with turbine models, when validated with observational data, can be used to evaluate the spatiotemporal accuracy of these mesoscale parameterizations. In this study, we compared the performance of the mesoscale wind-farm parameterization in the WRF model to that of a generalized actuator-disk model implemented in WRF-LES. The WFP produced wind profiles that were generally in agreement with GAD model output for both stability regimes. Small details were missed, however, including acceleration near the surface in stable conditions, the location of U_H and *TKE* maxima above hub-height, and asymptotic behavior in wake velocity deficits in the downwind half of the array that is indicative of wind-turbine array boundary layer development. In general, the WFP underestimated velocity deficits and overestimated *TKE* production (except for the NAT run, which underestimated wake turbulence). Neither increasing the vertical resolution in the rotor layer nor deactivating explicit *TKE* generation in the WFP produced clear advantages over the default mesoscale configuration. Parameterization performance was either on par or better for the 300 m grid resolution when compared to the 900 m resolution, but the general findings described herein apply for both domains. Finally, downwind power losses were overestimated by the WFP in stable conditions due to the lack of WTABL development.

Our results demonstrate that the WFP can qualitatively replicate the majority of wind speed and *TKE* impacts of a small LES-simulated turbine array. The significant overestimation of *TKE* generation at 300 m resolution suggests possible scaling issues with either the explicit turbulence source in the WFP, or the rate of turbulent mixing and dissipation in the WRF model physics. Future investigations could compare observed turbulence dissipation rates [*Lundquist and Bariteau*, 2015] with those simulated by LES and RANS wake models. The use of an explicit *TKE* source in the WFP appears justified, as downwind *TKE* production is nearly nonexistent otherwise, resulting in unphysical wake turbulence levels. The 300 m simulations do reveal spatial errors in WFP *TKE* production, however, as it appears from the GAD model runs that turbulence production maximizes in the cell immediately downwind of a turbine, rather than in the turbine cell itself.

We simulated an array of turbines in which each turbine is aligned in rows perpendicular to the mean wind direction, because this configuration is currently common among operational wind farms (based on visual inventory of U.S. wind-farm layouts). However, other array layouts could be simulated including staggered configurations and irregular grids. While layout differences are too small to be explicitly represented on a typical mesoscale model grid, estimates of the resulting uncertainty relative to LES simulations would

nonetheless be informative. We hypothesize that staggered and irregular layouts may produce a high bias in WFP wake impacts relative to the GAD model, as such layouts would tend to dampen velocity deficits and *TKE* production in LES simulations.

Many additional avenues exist for future comparison of mesoscale and LES representations of wind farms that build on the assessment presented herein. Time-varying mean flow fields could reveal the importance of yaw error. Model performance could be evaluated using real-world terrain and weather, though the use of nested LES domains in such configurations presents added challenges such as how to properly spin-up turbulence [*Muñoz-Esparza et al*., 2014]. Increased computing power would enable simulation of large LES wind farms, which could be used to evaluate wind-farm boundary layers deep within expansive arrays [*Meneveau*, 2012]. Of course, additional observation of wind-farm wake behavior could inform development of both techniques. In particular, comprehensive four-dimensional representations of flow throughout large arrays (e.g., from lidars [*Banta et al*., 2015; *Lundquist et al*., 2016] and radars [*Hirth et al*., 2015]) would enable validation of simulated wake evolution and structure. The myriad uses for wind-farm parameterizations present many challenges, but also many opportunities for evaluation and improvement.

Acknowledgments
The authors are thankful to Dr. Sven Schmitz and his research group at The Pennsylvania State University for generously providing turbine blade specifications of the PSU Generic 1.5-MW turbine. We also thank our reviewers, whose suggestions yielded new avenues of inquiry. This work was partially supported by the National Renewable Energy Laboratory under APUP UGA-0-41026-22 and by the National Science Foundation grant BCS-1413980 (Coupled Human Natural Systems). Our simulations were performed on the Janus supercomputer, which is supported by the National Science Foundation (award CNS-0821794), the University of Colorado Boulder, the University of Colorado Denver, and the National Center for Atmospheric Research. The Janus supercomputer is operated by the University of Colorado Boulder. The data used in this paper are available from the University of Colorado PetaLibrary (funded by NSF under grant OCI-1126839) and can be obtained from the corresponding author upon request.

References

Abkar, M., and F. Porté-Agel (2015a), A new wind-farm parameterization for large-scale atmospheric models, *J. Renewable Sustainable Energy*, *7*, 013121, doi:10.1063/1.4907600.

Abkar, M., and F. Porté-Agel (2015b), Influence of atmospheric stability on wind-turbine wakes: A large-eddy simulation study, *Phys. Fluids*, *27*, 035104, doi:10.1063/1.4913695.

Adams, A. S., and D. W. Keith (2013), Are global wind power resource estimates overstated?, *Environ. Res. Lett.*, *8*, 015021, doi:10.1088/1748-9326/8/1/015021.

Aitken, M. L., B. Kosović, J. D. Mirocha, and J. K. Lundquist (2014), Large eddy simulation of wind turbine wake dynamics in the stable boundary layer using the Weather Research and Forecasting model, *J. Renewable Sustainable Energy*, *6*, 033137, doi:10.1063/1.4885111.

Archer, C. L., and M. Z. Jacobson (2007), Supplying baseload power and reducing transmission requirements by interconnecting wind farms, *Am. Meteorol. Soc.*, *46*, 1701–1717, doi:10.1175/2007JAMC1538.1.

Archer, C. L., S. Mirzaeisefat, and S. Lee (2013), Quantifying the sensitivity of wind farm performance to array layout options using large-eddy simulation, *Geophys. Res. Lett.*, *40*, 4963–4970, doi:10.1002/grl.50911.

Baidya Roy, S. (2011), Simulating impacts of wind farms on local hydrometeorology, *J. Wind Eng. Ind. Aerodyn.*, *99*, 491–498, doi:10.1016/j.jweia.2010.12.013.

Baidya Roy, S., S. W. Pacala, and R. L. Walko (2004), Can large wind farms affect local meteorology?, *J. Geophys. Res.*, *109*, D19101, doi:10.1029/2004JD004763.

Banta, R. M., Y. L. Pichugina, W. A. Brewer, J. K. Lundquist, N. D. Kelley, S. P. Sandberg, R. J. Alvarez II, R. M. Hardesty, and A. M. Weickmann (2015), 3D volumetric analysis of wind turbine wake properties in the atmosphere using high-resolution Doppler lidar, *J. Atmos. Oceanic Technol.*, *32*, 904–914, doi:10.1175/JTECH-D-14-00078.1.

Barthelmie, R. J., G. C. Larsen, S. T. Frandsen, L. Folkerts, K. Rados, S. C. Pryor, B. Lange, and G. Schepers (2006), Comparison of wake model simulations with offshore wind turbine wake profiles measured by Sodar, *J. Atmos. Oceanic Technol.*, *23*, 888–901, doi:10.1175/JTECH1886.1.

Bhaganagar, K., and M. Debnath (2014), Implications of stably stratified atmospheric boundary layer turbulence on the near-wake structure of wind turbines, *Energies*, *7*, 5740–5763, doi:10.3390/en7095740.

Calaf, M., C. Meneveau, and J. Meyers (2010), Large eddy simulation study of fully developed wind-turbine array boundary layers, *Phys. Fluids*, *22*, 015110, doi:10.1063/1.3291077.

Calaf, M., M. B. Parlange, and C. Meneveau (2011), Large eddy simulation study of scalar transport in fully developed wind-turbine array boundary layers, *Phys. Fluids*, *23*, 126,603, doi:10.1063/1.3663376.

Cervarich, M. C., S. Baidya Roy, and L. Zhou (2013), Spatiotemporal structure of wind farm-atmospheric boundary layer interactions, *Energy Proc.*, *40*, 530–536, doi:10.1016/j.egypro.2013.08.061.

Churchfield, M. J., S. Lee, J. Michalakes, and P. J. Moriarty (2012a), A numerical study of the effects of atmospheric and wake turbulence on wind turbine dynamics, *J. Turbul.*, *13*, 1–32, doi:10.1080/14685248.2012.668191.

Churchfield, M. J., S. Lee, P. J. Moriarty, L. A. Martínez, S. Leonardi, G. Vijayakumar, and J. G. Brasseur (2012b), A large-eddy simulation of wind-plant aerodynamics, paper presented at 50th AIAA Aerospace Sciences Meeting including the New Horizons Forum and Aerospace Exposition, American Institute of Aeronautics and Astronautics, Nashville, Tenn.

Crespo, A., J. Hernández, and S. Frandsen (1999), Survey of modelling methods for wind turbine wakes and wind farms, *Wind Energy*, *2*, 1–24, doi:10.1002/(SICI)10991824(199901/03)2:1<1::AID-WE16>3.0.CO;2-7.

Dörenkämper, M., B. Witha, G. Steinfeld, D. Heinemann, and M. Kühn (2015), The impact of stable atmospheric boundary layers on wind-turbine wakes within offshore wind farms, *J. Wind Eng. Ind. Aerodyn.*, *144*, 146–153, doi:10.1016/j.jweia.2014.12.011.

Fiedler, B. H., and M. S. Bukovsky (2011), The effect of a giant wind farm on precipitation in a regional climate model, *Environ. Res. Lett.*, *6*, 045101, doi:10.1088/1748-9326/6/4/045101.

Fitch, A. C. (2015a), Climate impacts of large-scale wind farms as parameterized in a global climate model, *J. Clim.*, *28*, 6160–6180, doi:10.1175/JCLI-D-14-00245.1.

Fitch, A. C. (2015b), Notes on using the mesoscale wind farm parameterization of Fitch et al. (2012) in WRF, *Wind Energy*, 19, 1757–1758, doi:10.1002/we.1945.

Fitch, A. C., J. B. Olson, J. K. Lundquist, J. Dudhia, A. K. Gupta, J. Michalakes, and I. Barstad (2012), Local and mesoscale impacts of wind farms as parameterized in a mesoscale NWP model, *Mon. Weather Rev.*, *140*, 3017–3038, doi:10.1175/MWR-D-11-00352.1.

Fitch, A. C., J. K. Lundquist, and J. B. Olson (2013a), Mesoscale influences of wind farms throughout a diurnal cycle, *Mon. Weather Rev.*, *141*, 2173–2198, doi:10.1175/MWR-D-12-00185.1.

Fitch, A. C., J. B. Olson, and J. K. Lundquist (2013b), Parameterization of wind farms in climate models, *J. Clim.*, *26*, 6439–6458, doi:10.1175/JCLI-D-12-00376.1.

Hirth, B. D., J. L. Schroeder, W. S. Gunter, and J. G. Guynes (2015), Coupling Doppler radar-derived wind maps with operational turbine data to document wind farm complex flows, *Wind Energy*, *18*, 529–540, doi:10.1002/we.1701.

Jacobson, M. Z., and C. L. Archer (2012), Saturation wind power potential and its implications for wind energy, *Proc. Natl. Acad. Sci. U. S. A.*, *109*, 15,679–15,684, doi:10.1073/pnas.1208993109.

Jimenez, A., A. Crespo, E. Migoya, and J. Garcia (2007), Advances in large-eddy simulation of a wind turbine wake, *J. Phys. Conf. Ser.*, *75*, 012041, doi:10.1088/1742-6596/75/1/012041.

Jimenez, A., A. Crespo, E. Migoya, and J. Garcia (2008), Large-eddy simulation of spectral coherence in a wind turbine wake, *Environ. Res. Lett.*, *3*, 015004, doi:10.1088/1748-9326/3/1/015004.

Jiménez, P. A., J. Javarro, A. M. Palomares, and J. Dudhia (2015), Mesoscale modeling of offshore wind turbine wakes at the wind farm resolving scale: A composite-based analysis with the Weather Research and Forecasting model over Horns Rev, *Wind Energy*, *18*, 559–566, doi:10.1002/we.1708.

Kaffine, D. T., and C. M. Worley (2010), The windy commons?, *Environ. Resour. Econ.*, *47*, 151–172, doi:10.1007/s10640-010-9369-2.

Keith, D., J. DeCarolis, D. Denkenberger, D. Lenschow, S. Malyshev, S. Pacala, and P. J. Rasch (2004), The influence of large-scale wind power on global climate, *Proc. Natl. Acad. Sci. U. S. A.*, *101*, 16,115–16,120, doi:10.1073/pnas.0406930101.

Kirk-Davidoff, D. B., and D. W. Keith (2008), On the climate impact of surface roughness anomalies, *J. Atmos. Sci.*, *65*, 2215–2234, doi:10.1175/2007JAS2509.1.

Kirkil, G., J. D. Mirocha, F. K. Chow, and E. Bou-Zeid (2012), Implementation and evaluation of dynamic subfilter-scale stress models for large-eddy simulation using WRF, *Mon. Weather Rev.*, *140*, 266–284, doi:10.1175/MWR-D-11-00037.1.

Kosović, B. (1997), Subgrid-scale modeling for large-eddy simulations of high-Reynolds-number boundary layers, *J. Fluid Mech.*, *336*, 151–182, doi:10.1017/S0022112096004697.

Lu, H., and F. Porté-Agel (2011), Large-eddy simulation of a very large wind farm in a stable atmospheric boundary layer, *Phys. Fluids*, *23*, 065101, doi:10.1063/1.3589857.

Lu, X., M. B. McElroy, and J. Kiviluoma (2009), Global potential for wind-generated electricity, *Proc. Natl. Acad. Sci. U. S. A.*, *106*, 10,933–10,938, doi:10.1073/pnas.0904101106.

Lundquist, K. A., F. K. Chow, and J. K. Lundquist (2012), An immersed boundary method enabling large-eddy simulations of urban terrain in the WRF model, *Mon Weather Rev.*, *140*, 3936–3955, doi:10.1175/MWR-D-11-00311.1.

Lundquist, J. K., and L. Bariteau (2015), Dissipation of Turbulence in the Wake of a Wind Turbine, *Boundary-Layer Meteorol.*, *154*, 229–241, doi:10.1007/s10546-014-9978-3.

Lundquist, J. K., et al. (2016), Assessing state-of-the-art capabilities for probing the atmospheric boundary layer: The XPIA field campaign, *Br. Am. Meteorol. Soc.*, doi:10.1175/BAMS-D-15-00151.1.

Mahrt, L. (2014), Stably stratified atmospheric boundary layers, *Annu. Rev. Fluid Mech.*, *46*, 23–45, doi:10.1146/annurev-fluid-010313-141354.

Marvel, K., B. Kravitz, and K. Caldeira (2013), Geophysical limits to global wind power, *Nat. Clim. Change*, *3*, 118–121, doi:10.1038/nclimate1683.

Meneveau, C. (2012), The top-down model of wind farm boundary layers and its applications, *J. Turbul.*, *13*, N7, doi:10.1080/14685248.2012.663092.

Meyers, J., and C. Meneveau (2012), Optimal turbine spacing in fully developed wind farm boundary layers, *Wind Energy*, *15*, 305–317, doi:10.1002/we.469.

Mirocha, J. D., J. K. Lundquist, and B. Kosović (2010), Implementation of a nonlinear subfilter turbulence stress model for large-eddy simulation in the Advanced Research WRF model, *Mon. Weather Rev.*, *138*, 4212–4228, doi:10.1175/2010MWR3286.1.

Mirocha, J. D., G. Kirkil, E. Bou-Zeid, F. K. Chow, and B. Kosović (2013), Transition and equilibration of neutral atmospheric boundary layer flow in one-way nested large eddy simulations using the weather research and forecasting model, *Mon. Weather Rev.*, *141*, 918–940, doi:10.1175/MWR-D-11-00263.1.

Mirocha, J. D., B. Kosović, M. L. Aitken, and J. K. Lundquist (2014), Implementation of a generalized actuator disk wind turbine model into the weather research and forecasting model for large-eddy simulation applications, *J. Renewable Sustainable Energy*, *6*, 013104, doi:10.1063/1.4861061.

Mirocha, J. D., D. A. Rajewski, N. Marjanovic, J. K. Lundquist, B. Kosović, C. Draxl, and M. J. Churchfield (2015), Investigating wind turbine impacts on near-wake flow using profiling lidar data and large-eddy simulations with an actuator disk model, *J. Renewable Sustainable Energy*, *7*, 043143, doi:10.1063/1.4928873.

Moeng, C.-H., J. Dudhia, J. B. Klemp, and P. P. Sullivan (2007), Examining two-way nesting for large eddy simulation of the PBL using the WRF model, *Mon. Weather Rev.*, *135*, 2295–2311, doi:10.1175/MWR3406.1.

Muñoz-Esparza, D., B. Kosović, J. Mirocha, and J. van Beeck (2014), Bridging the transition from mesoscale to microscale turbulence in numerical weather prediction models, *Boundary Layer Meteorol.*, *153*, 409–440, doi:10.1007/s10546-014-9956-9.

Nygaard, N. G. (2014), Wakes in very large wind farms and the effect of neighbouring wind farms, *J. Phys. Conf. Ser.*, *524*, 012162, doi:10.1088/1742-6596/524/1/012162.

Rajewski, D. A., E. S. Takle, J. K. Lundquist, J. H. Prueger, R. L. Pfeiffer, J. L. Hatfield, K. K. Spoth, and R. K. Doorenbos (2014), Changes in fluxes of heat, H_2O, and CO_2 caused by a large wind farm, *Agric. For. Meteorol.*, *194*, 175–187, doi:10.1016/j.agrformet.2014.03.023.

Schmitz, S. (2012), XTURB-PSU: A wind turbine design and analysis tool, Department of Aerospace Engineering, Penn State University, State College, Pa. [http://www.aero.psu.edu/Faculty_Staff/schmitz/XTurb/XTurb.html]

Skamarock, W. C., J. B. Klemp, J. Dudhia, D. O. Gill, D. M. Barker, M. G. Duda, X. Huang, W. Wang, and J. G. Powers (2008), A description of the advanced research WRF version 3, *Tech. Note NCAR/TN-475+STR*, 125 pp., Nat. Cent. Atmos. Res., Boulder, Colo.

St. Martin, C. M., J. K. Lundquist, and M. A. Handschy (2015), Variability of interconnected wind plants: Correlation length and its dependence on variability time scale, *Environ. Res. Lett.*, *10*, 044004, doi:10.1088/1748-9326/10/4/044004.

Stull, R. B. (1988), *An Introduction to Boundary Layer Meteorology*, 670 pp., Kluwer, Dordrecht.

Troldborg, N., J. N. Sorensen, and R. Mikkelsen (2010), Numerical simulations of wake characteristics of a wind turbine in uniform inflow, *Wind Energy*, *13*, 86–99, doi:10.1002/we.345.

Troldborg, N., G. C. Larsen, H. A. Madsen, K. S. Hansen, J. N. Sørensen, and R. Mikkelsen (2011), Numerical simulations of wake interaction between two wind turbines at various inflow conditions, *Wind Energy*, *14*, 859–876, doi:10.1002/we.433.

Vanderwende, B. J., and J. K. Lundquist (2012), The modification of wind turbine performance by statistically distinct atmospheric regimes, *Environ. Res. Lett.*, *7*, 034035, doi:10.1088/1748-9326/7/3/034035.

Vanderwende, B. J., and J. K. Lundquist (2015), Could crop height affect the wind resource at agriculturally productive wind farm sites?, *Boundary Layer Meteorol.*, *158*, 409–428, doi:10.1007/s10546-015-0102-0.

Vautard, R., F. Thais, I. Tobin, F. M. Bréon, J. G. D. de Lavergne, A. Colette, P. Yiou, and P. M. Ruti (2014), Regional climate model simulations indicate limited climatic impacts by operational and planned European wind farms, *Nat. Commun.*, *5*, 3196, doi:10.1038/ncomms4196.

Vollmer, L., M. van Dooren, D. Trabucchi, J. Schneemann, G. Steinfeld, B. Witha, J. Trujillo, and M. Kühn (2015), First comparison of LES of an offshore wind turbine wake with dual-Doppler lidar measurements in a German offshore wind farm, *J. Phys. Conf. Ser.*, *625*, 012001, doi:10.1088/1742-6596/625/1/012001.

Wang, C., and R. G. Prinn (2011), Potential climatic impacts and reliability of large-scale offshore wind farms, *Environ. Res. Lett.*, *6*, 025101, doi:10.1088/1748-9326/6/2/025101.

Wharton, S., and J. K. Lundquist (2012), Assessing atmospheric stability and its impacts on rotor-disk wind characteristics at an onshore wind farm, *Wind Energy*, *15*, 525–546, doi:10.1002/we.483.

Wyngaard, J. C. (2004), Toward numerical modeling in the "terra incognita", *J. Atmos. Sci.*, *61*, 1816–1826, doi:10.1175/1520-0469(2004)061<1816:TNMITT>2.0.CO;2.